

Low velocity impact response of 3D printed layered structures formed by cellular metamaterials and stiffening plates

F.A. Santos^{a,*}, H. Rebelo^b, M. Coutinho^c, L.S. Sutherland^d, C. Cismasiu^a, R. Luciano^e and F. Fraternali^f

^aCERIS and Departamento de Engenharia Civil da Faculdade de Ciências e Tecnologia, Universidade NOVA de Lisboa, Quinta da Torre, 2829-516 Caparica, Portugal

^bCINAMIL and Departamento de Engenharia Civil da Faculdade de Ciências e Tecnologia, Universidade NOVA de Lisboa, Quinta da Torre, 2829-516 Caparica, Portugal

^cDepartamento de Engenharia Civil da Faculdade de Ciências e Tecnologia, Universidade NOVA de Lisboa, Quinta da Torre, 2829-516 Caparica, Portugal

^dCENTEC and Instituto Superior Técnico, Universidade de Lisboa, Lisboa, 1049-001, Portugal

^eDepartment of Engineering, University of Naples "Parthenope", 80143 Naples (Italy)

^fDepartment of Civil Engineering, University of Salerno, 84084 Fisciano(SA), Italy

ARTICLE INFO

Keywords:

cellular metamaterials
3D printing
Low velocity impact
PLA
PETg
Auxetic

ABSTRACT

The present paper studies the low-velocity impact response of 3D-printed layered structures made of thermoplastic materials (PLA and PETg), to be employed as sacrificial cladding for the protection of materials and structures. The analyzed layered structures are composed of crushable cellular cores placed in between terminal stiffening plates. The cores tessellate either regular hexagonal unit cells, or hexagonal cells with re-entrant corners, with the latter exhibiting auxetic response. The given results highlight that the examined PETg structures show superior impact response over the PLA counterparts featuring same geometry. It is concluded that PETg qualifies as a convenient material for the fabrication of novel impact protection gear made of cellular sacrificial cladding, which can be conveniently fabricated through ordinary, low-cost 3D printers.

1. Introduction

Recent advances in additive manufacturing technologies have provided for unprecedented means to develop tailored engineered metamaterials for protective solutions against impact loads, namely through lightweight sacrificial cladding, impossible to obtain with traditional subtractive manufacturing techniques [16, 2, 5, 7, 8, 14, 13, 12, 17]. Fused deposition modeling extrusion based technique (FDM) is the most widespread 3D printing technology, available in consumer-level 3D printers. This technique resorts to a spool of thermoplastic filament to be melted and extruded through a heated nozzle and, subsequently, deposited in two-dimensional layers that will form a 3D component [3]. A sacrificial cladding is usually composed of a crushable core placed in between two plates. With the FDM technique, one can easily customize the topology of the cellular core and optimize its structural performance regarding a specific design parameter, i.e. stiffness, energy dissipation and resilience towards high deformations. The enormous popularity of FDM technology as a rapid prototyping tool has fostered important research outcomes regarding the mechanical characterization of different cellular geometries, paving way to the fast dissemination of new and exciting metamaterials, with fascinating properties [8]. The most widespread unit cell topologies used in engineered sacrificial cladding for protective solutions, are the hexagonal cell and the hexagonal based cell with re-entrant corners, featuring auxetic behavior [5, 14,

13, 10, 18, 11, 6]. Auxetic metamaterials have been shown to present the capacity to sustain very high deformations under a constant low stress, mainly due to their compliant nature. Hexagonal honeycomb based sacrificial cladding, on the other hand, are ultra-stiff structures which can accommodate large plastic damage while dissipating a significant amount of energy. As the performance of such metamaterials in protective solutions against impact loads mostly derives from the geometry of their cellular cores, most studies regarding this type of applications are focused on the shape optimization of the cells, rather than on the material itself. Polylactic acid (PLA) is a thermoplastic polyester which is both inexpensive and easy to print, with a widespread application in consumer-level 3D printers. For these reasons, PLA is very popular among researchers and is often used in 3D-printed sacrificial cladding solutions based in cellular metamaterials [16, 9, 12]. However, much like other synthetic plastics, PLA has its own inherent weakness, in particular, its low toughness, which is translated into its poor ability to absorb sudden impact energy without breaking. In fact, PLA is a brittle polymer, with low crack initiation energy, hindering its performance in protective applications aiming to mitigate impact. With its higher flexibility and increased toughness, polyethylene terephthalate glycol-modified (PETg) 3D-printing filament presents itself as a potential candidate to replace PLA in protective applications.

In the present study, the low-velocity impact response of 3D-printed sacrificial cladding is addressed, using specimens manufactured with both PLA and PETg filaments. All specimens were manufactured from single spools of com-

 fpas@fct.unl.pt (F.A. Santos)

ORCID(s):

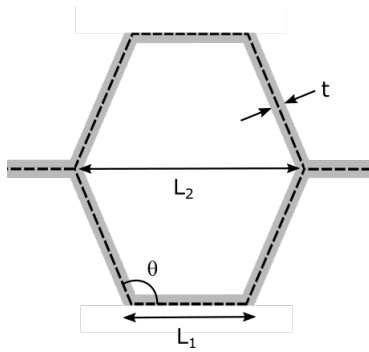
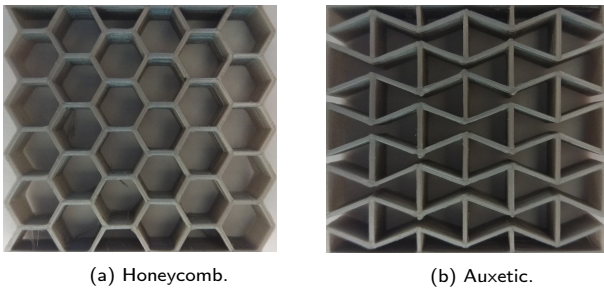


Figure 1: Unitary hexagonal cell.



(a) Honeycomb.

(b) Auxetic.

Figure 2: Structures of the cellular cores.

mercial PLA and PETg laments, using a Prusa i3 MK2 printer. The laments with a diameter of 1.75 mm, were extruded through a 0.4 mm diameter nozzle and deposited layer by layer according to a user dened pattern, in order to obtain the desired 3D specimen. Two cellular topologies were used, based in the unitary hexagonal cell represented in Figure 1. By setting the parameters L_1 , L_2 , θ and t according to the values shown in Table 1 it is possible to obtain a relative density of 25% for both the cellular geometries shown in Figures 2(a) and (b), which are the hexagonal (honeycomb) structure and the hexagonal-based structure with re-entrant corners, showing auxetic behavior, respectively. The sacri-

Table 1

Geometric parameters of the hexagonal cell.

	L_1 (mm)	L_2 (mm)	θ (degrees)	t (mm)
Honeycomb	5	5	120	1
Auxetic	5	5	70	0.8

ficial cladding specimens were materialized by $100 \times 100 \times 50 \text{ mm}^3$ blocks comprising cellular, crushable, cores sandwiched between two 5 mm plates. In Figure 3 and Figure 4 are presented the honeycomb and the auxetic sacrificial cladding, respectively. The printing parameters used to make all the 3D-printed specimens in the present study are listed in Table 2.

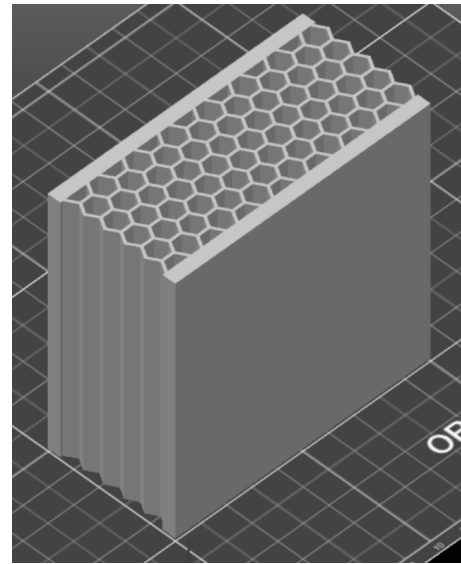


Figure 3: Honeycomb sacrificial cladding.

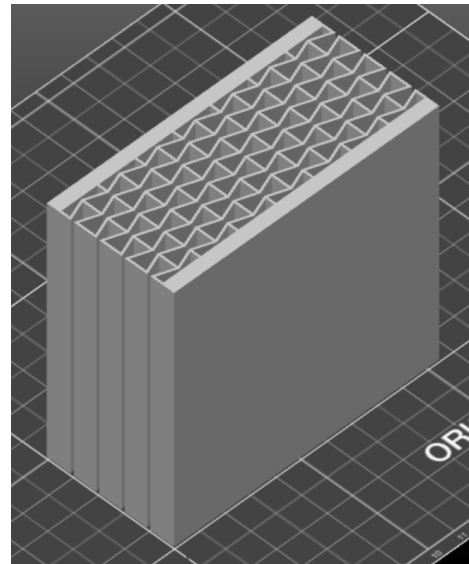


Figure 4: Auxetic sacrificial cladding.

2. Uniaxial tensile tests

The ASTM D638 Standard Test Methods for Tensile Properties of Plastics [1] was used to characterize the plastic strength specifications related to the tensile properties of PLA and PETg. Three standard “dogbone” shaped specimens (Type IV) of each material were printed. The specimens were printed with 100% infill and a raster orientation of 45 degrees (see Figure 5). Each specimen was individually measured (thickness and width) at several locations. In Table 3 is compiled the information regarding the mass and dimensions of the 3D-printed specimens. The tensile tests were performed with Zwick/Roell Z50 universal testing machine, with a strain-rate of 0.1%/s, using a gauge length of 50mm to measure the strains of the 3D-printed specimen, as shown in Figure 6. In Figure 7 are presented the force-displacement diagrams

Table 2
 Printing parameters.

	PLA	PETg
Nozzle extrusion temperature	210 ° C	250 ° C
Heated bed temperature	60 ° C	50 ° C
Layer height	0.2 mm	0.2 mm
Printing speed	30 mm/s	30 mm/s
Number of outer shells	2	2

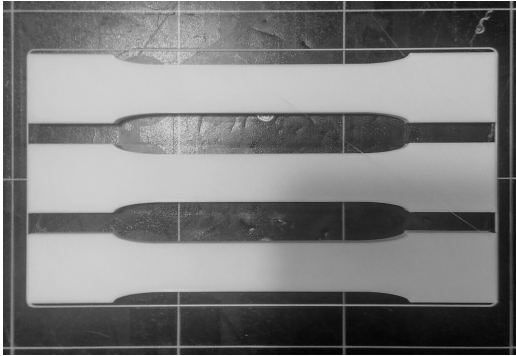

Figure 5: 3d-printed specimen.

Table 3
 Tensile testing of 3d-printed specimen.

	M (g)	L_1 (mm)	L_2 (mm)
PLA 1	15.81	14.22	6.35
PLA 2	15.84	14.09	6.41
PLA 3	15.80	14.20	6.42
PETg 1	16.51	14.01	6.09
PETg 2	16.16	14.07	6.17
PETg 3	16.17	13.87	6.18

obtained during the tensile tests for both the PLA and PETg specimens. In Table 4 are compiled the mechanical properties obtained for the PLA and PETg specimens. According to the obtained results one can see that the tensile toughness of the PLA specimens is higher than that of its PETg counterparts, which are also more flexible. Tensile toughness results from a combination of strength and ductility and is translated into the ability of the specimen to absorb energy while subjected to tension. This higher toughness showed by the PLA specimens seems to be in contradiction with the fact that PLA bulk material is more brittle than PETg. As already extensively studied in the literature, the mechanical properties of components manufactured through FDM technology may vary significantly from those of the bulk materials, markedly depending on the printing process parameters.

3. Quasi-static tests

Quasi-static (QS) tests were carried out on an instrumented servo-hydraulic test machine at a constant rate of displacement, using a hemispherical ended cylindrical impact

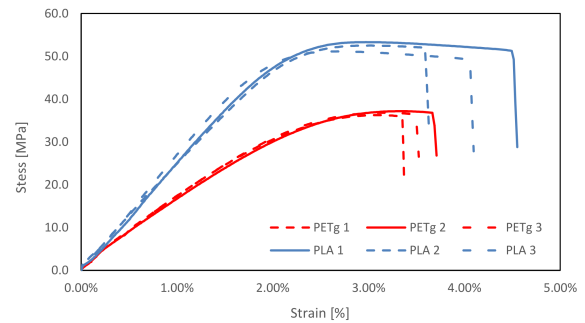

Figure 6: Tensile testing procedure.

Figure 7: Force-displacement diagrams.

Table 4
 Tensile testing of 3d-printed specimen.

	σ_y (MPa)	σ_u (MPa)	ϵ_y (%)	ϵ_u (%)	E (GPa)
PLA 1	53.1	51.3	2.31	4.51	2.77
PLA 2	52.2	50.1	2.36	3.63	2.75
PLA 3	51.0	49.3	2.55	3.71	2.74
PETg 1	34.01	36.8	2.31	3.67	1.81
PETg 2	34.10	37.2	2.33	3.37	1.80
PETg 3	34.45	36.5	2.29	3.48	1.82
PLA (avg)	52.10	50.23	2.41	3.95	2.75
PLA (sd)	1.05	1.01	0.13	0.49	0.02
PETg (avg)	34.19	36.83	2.31	2.31	1.81
PETg (sd)	0.23	0.35	0.02	0.02	0.01

head with 30 mm diameter (see Figure 8) [15, 4]. The specimens were simply supported on a steel apparatus with an outside diameter of 100 mm and a central circular hole with 50 mm diameter. In Figure 9 are shown the hexagonal cladding during the quasi-static loading, for both PETg and PLA materials. The frame that is depicted corresponds to the moment when the maximum force is attained, before the densi-

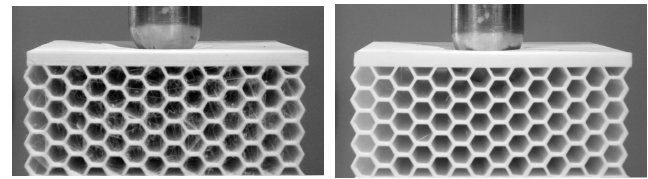


Figure 8: Servo-hydraulic test machine.

fication process starts. In Figures 10 and 11 are shown the force-displacement and absorbed energy-displacement diagrams for the hexagonal cladding, respectively. According to Figure 9 one can see that the hexagonal cladding shows a similar deformation pattern for both materials, with the deformations mainly concentrated within the vicinity of the impact head. As it can be seen in Figure 10, the maximum forces before densification are reached for a vertical displacement of the impact head of 4 mm, with the PETg cladding denoting increased flexibility. The PETg cladding resisted to a maximum force, before densification, of 4.0 kN while the PLA cladding resisted to a force of 6.5 kN. Additionally to higher strength, the PLA cladding also showed higher energy absorption capacities, as shown in Figure 11.

In Figure 12 are shown the auxetic cladding during the quasi-static loading, for both PETg and PLA materials. One can clearly see the development of the auxetic effect during loading, with the core material moving towards the impact head. In Figures 13 and 14 are shown the force-displacement and absorbed energy-displacement diagrams for the auxetic cladding, respectively. Regarding the behavior of the auxetic cladding both materials showed an outstanding capacity to accommodate large, recoverable, displacements, with similar maximum elastic displacement values for both materials, around 14 mm, which are 3.5 times higher than the maximum elastic displacements obtained for the hexagonal cores. PLA denoted a stiffer response, reaching higher force levels than the PETg auxetic core. The maximum force value for the PLA material was 6.5 kN while with PETg this value was limited to 4.0 kN. Actually, these force values are quite similar to the ones obtained with the hexagonal cores. In terms of absorbed energy, The PLA auxetic core was able to absorb around 30 % more energy than the PETg core during the elastic response phase of the cladding.

During the QS tests it was also possible to assess the Poisson coefficient of the hexagonal and auxetic cladding. Both vertical and horizontal displacements were evaluated



(a) PETg.

(b) PLA.

Figure 9: Quasi-static tests (hexagonal)

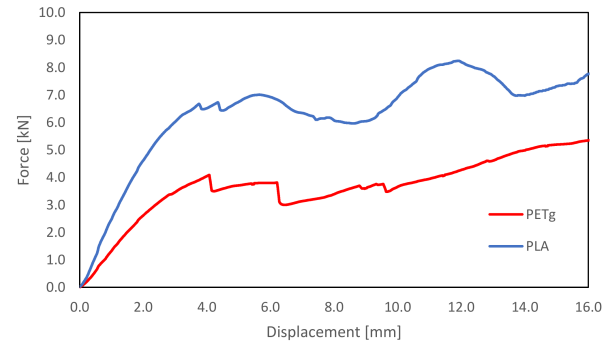


Figure 10: Force-displacement diagram (hexagonal).

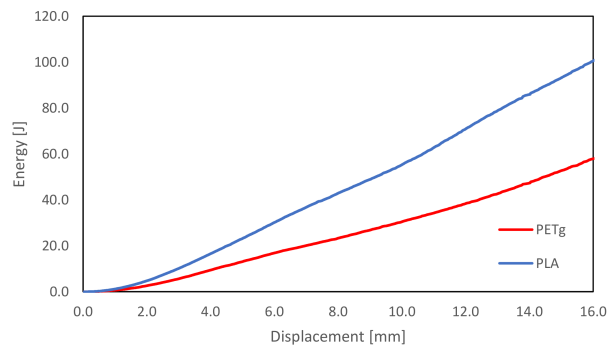


Figure 11: Absorbed energy-displacement (hexagonal).

by digital image processing, in the linear branch of the cladding force-displacement responses. In Table 5 are shown the computed values for the Poisson coefficients of the cladding, which yielded 0.19 and - 0.38 for the hexagonal and auxetic structures, respectively.

Table 5
Poisson coefficient.

	Hexagonal	Auxetic
Vertical displacement [mm]	1.00	1.00
Horizontal displacement [mm]	0.19	- 0.38
Poisson coefficient	0.19	- 0.38

4. Low-velocity dynamic tests

Impact testing was performed using a fully instrumented Rosand IFW5 falling weight machine Figure 15 [4]. The hemispherical ended cylindrical impact head, which was also used in QS tests, is dropped from a known, variable height

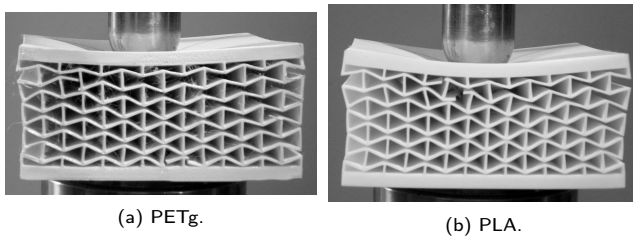


Figure 12: Quasi-static tests (auxetic)

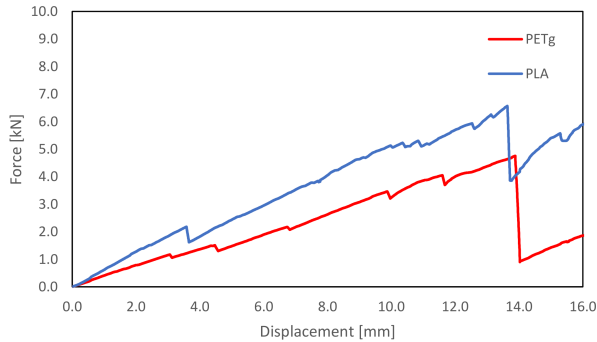


Figure 13: Force-displacement diagram (auxetic).

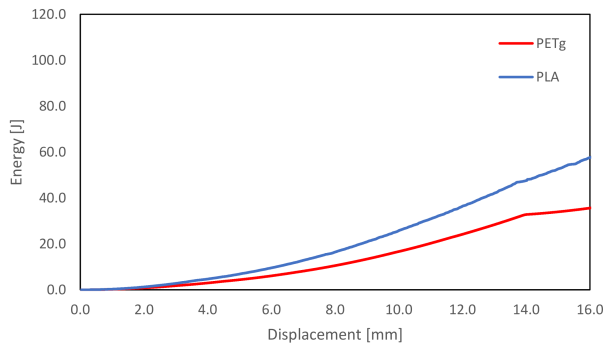


Figure 14: Absorbed energy-displacement (auxetic).

between guide rails onto the horizontally supported 3D printed cladding. A much larger, variable mass is attached to the impact head and a load cell between the two gives the variation of impact force with time. The data is post-filtered to remove noise from the signal. An optical gate provides the incident velocity of the impact head. The time histories of the displacement, the absorbed energy and the velocity are calculated from the measured force-time data by numerical integration. A Photron Fastcam Mini Ax high speed camera (HSC) is used at a frame rate of 10,000 frames per second and a resolution of 768 by 528 pixel. All measurements were synchronized using a light intensity trigger. Two levels of incident kinetic energy were used during the tests, namely 10 J and 20 J. In Figures 16 through 19 are shown the results obtained for the low-velocity impact tests regarding the hexagonal core cladding subjected to an incident kinetic energy of 10 J. In Figures 16 (a) and (b) are depicted two time frames of the tests, t_1 and t_2 , which correspond to the instants associated with the maximum force and the maximum displacement before rebound, respectively. It is possible to see



Figure 15: Rosand IFW5 instrumented falling weight impact tester.

that both cladding suffered very limited deformation with the PLA specimen showing no plastic damage. In fact, in the force-displacement diagram in Figure 17, the PLA specimen presents a maximum displacement of 3.2 mm with no residual deformation after impact. The maximum force transmitted to the PLA specimen was around 6.0 kN. The PETg specimen sustained a light damage, with a maximum displacement of 5.6 mm, while limiting the transmitted force to 3.2 kN. In Figure 18 is shown the response of the cladding in terms of absorbed and dissipated energy. While the absorbed energy is similar for both specimens, corresponding to the kinetic energy introduced in the system (maximum energy value in the graph), the dissipated energy (value of the horizontal plateau in right-hand side of the graph) is quite different. In fact, while in the PETg cladding the dissipated energy is about 90% of the absorbed energy, in the PLA cladding this ratio drops-off to only 45%. In Figure 19 is shown the velocity response of the impactor head during dynamic tests with the PETg cladding leading to significantly lower velocities than its PLA counterpart. Defining the restitution coefficient as $|v_{out}|/|v_{in}|$, with v_{in} being the velocity at the time of impact and v_{out} being the rebound velocity of the impactor head, one can say that the restitution coefficients for the PLA and PETg cladding are 74% and 32%, respectively. As the PETg cladding dissipates more energy during impact the rebound velocity of the impactor head is lower.

In Figures 20 through 23 are shown the results obtained for the low-velocity impact tests regarding the auxetic core cladding subjected to an incident kinetic energy of 10 J. In this case, both specimens suffered moderate damage, with the cladding demonstrating the capacity of auxetic structures to accommodate high displacements while controlling the transmitted forces. The general trend of the responses ob-

tained during this test is quite similar to the ones obtained for the hexagonal cladding, in what concerns the performance of the PLA and PETg materials. In the force-displacement diagram in Figure 21, the PLA specimen presents a maximum displacement of 7.5, with a maximum force of 2.3 kN. The PETg specimen showed a maximum displacement of 9.7 mm, while limiting the transmitted force to 1.8 kN. In Figure 22 is shown the response of the auxetic cladding in terms of absorbed and dissipated energy. In the PETg cladding the dissipated energy amounts to 83% of the absorbed energy while in the PLA cladding this ratio is 71%. In Figure 23 is shown the velocity response of the impactor head during dynamic tests with the PETg cladding leading to lower velocities than its PLA counterpart. In this case the restitution coefficients for the PLA and PETg cladding are 53% and 40%, respectively.

In Figures 24 through 31 is shown the overall response of the cladding during the low-velocity impact tests, subjected to an incident kinetic energy of 20 J. In these tests, the amount of damage inflicted to the test specimens is very extensive, especially in the case of the auxetic cladding. Increased plastic damage is translated into higher energy dissipation ratios and also lower restitution coefficients.

5. Discussion

The results obtained during the low-velocity dynamic tests have clearly demonstrated that for both the considered cellular cores, hexagonal and auxetic, PETg material has fostered higher energy dissipation capabilities for the cladding, also translated into lower restitution coefficients. The higher flexibility of PETg has led to higher deformations than PLA, while limiting the force which is transmitted to the cladding to lower values. This highlights the best overall performance of PETg in sacrificial cladding build up of cellular cores and paves way to new protective applications regarding the use of this material. In Figures 32 through 35 is showed a compilation of the data obtained during the quasi-static and low-velocity dynamic tests. In Figure 32 is presented the maximum force transmitted to the cladding by the impactor head during both tests. One can see that QS tests can actually give a very good estimation of the maximum force transmitted by the cladding, for a given energy input, for the hexagonal configuration. For the auxetic configuration, the QS tests still yields a good estimate of the force for the 10 J scenario, while for the 20 J scenario this estimation is no longer valid. A similar trend can be seen in Figure 33, regarding the maximum displacement shown by the specimens. The QS tests give reasonable good estimates of the maximum displacement for the hexagonal core and also for the auxetic core for the 10 J energy input scenario. In Figures 34 and 35 are compiled the obtained energy dissipation ratios and the corresponding restitution coefficients.

6. Conclusions

This paper addresses the low-velocity impact response of 3D-printed sacrificial cladding using specimens manu-

factured with both PLA and PETg filaments. From the performed analysis one can highlight the following conclusions:

1. PETg material has fostered higher energy dissipation capabilities for the cladding, showing lower restitution coefficients.
2. The higher flexibility of PETg has led to higher deformations than PLA, while limiting the force which is transmitted to the cladding to lower values.
3. For limited energy input, QS tests can give a very good estimation of the maximum force transmitted by the cladding.
4. The best overall performance of PETg in sacrificial cladding build up of cellular cores paves way to new protective applications regarding the use of this material.

References

- [1] ASTM D638-14, 2014. Standard Test Method for Tensile Properties of Plastics. Technical Report. West Conshohocken, PA.
- [2] Debeau, D.A., Seepersad, C.C., Haberman, M.R., 2018. Impact behavior of negative stiffness honeycomb materials. *Journal of Materials Research* 33, 290–299. doi:10.1557/jmr.2018.7.
- [3] Dizon, J.R.C., Espera, A.H., Chen, Q., Advincula, R.C., 2018. Mechanical characterization of 3D-printed polymers. *Additive Manufacturing* 20, 44–67. doi:https://doi.org/10.1016/j.addma.2017.12.002.
- [4] Garrido, M., Teixeira, R., Correia, J.R., Sutherland, L.S., 2019. Quasi-static indentation and impact in glass-fibre reinforced polymer sandwich panels for civil and ocean engineering applications. *Journal of Sandwich Structures & Materials*, 1099636219830134doi:10.1177/1099636219830134.
- [5] Hou, S., Li, T., Jia, Z., Wang, L., 2018. Mechanical properties of sandwich composites with 3d-printed auxetic and non-auxetic lattice cores under low velocity impact. *Materials & Design* 160, 1305–1321. doi:10.1016/j.matdes.2018.11.002.
- [6] Hu, L.L., Zhou, M.Z., Deng, H., 2019. Dynamic indentation of auxetic and non-auxetic honeycombs under large deformation. *Composite Structures* 207, 323–330. doi:10.1016/j.compstruct.2018.09.066.
- [7] Imbalzano, G., Linforth, S., Ngo, T.D., Lee, P.V.S., Tran, P., 2018. Blast resistance of auxetic and honeycomb sandwich panels: Comparisons and parametric designs. *Composite Structures* 183, 242–261. doi:10.1016/j.compstruct.2017.03.018.
- [8] Jiang, Y., Li, Y., 2018. 3D printed auxetic mechanical metamaterial with chiral cells and re-entrant cores. *Scientific reports* 8, 1–11. doi:10.1038/s41598-018-20795-2.
- [9] Kao, Y.T., Amin, A.R., Payne, N., Wang, J., Tai, B.L., 2018. Low-velocity impact response of 3D-printed lattice structure with foam reinforcement. *Composite Structures* 192, 93–100. doi:10.1016/j.compstruct.2018.02.042.
- [10] Novak, N., Starčević, L., Vesenjčak, M., Ren, Z., 2019. Blast response study of the sandwich composite panels with 3D chiral auxetic core. *Composite Structures* 210, 167–178. doi:10.1016/j.compstruct.2018.11.050.
- [11] Qi, C., Remennikov, A., Pei, L.Z., Yang, S., Yu, Z.H., Ngo, T.D., 2017. Impact and close-in blast response of auxetic honeycomb-cored sandwich panels: experimental tests and numerical simulations. *Composite structures* 180, 161–178. doi:10.1016/j.compstruct.2017.08.020.
- [12] Rebelo, H.B., Lecomte, D., Cismasiu, C., Jonet, A., Belkassam, B., Maazoun, A., 2019. Experimental and numerical investigation on 3D printed PLA sacrificial honeycomb cladding. *International Journal of Impact Engineering* 131, 162–173. doi:10.1016/j.ijimpeng.2019.05.013.
- [13] Sarvestani, H.Y., Akbarzadeh, A.H., Mirbolghasemi, A., Hermenean, K., 2018a. 3D printed meta-sandwich structures: Failure mechanism,

- energy absorption and multi-hit capability. *Materials & Design* 160, 179–193. doi:<https://doi.org/10.1016/j.matdes.2018.08.061>.
- [14] Sarvestani, H.Y., Akbarzadeh, A.H., Niknam, H., Hermenean, K., 2018b. 3D printed architected polymeric sandwich panels: Energy absorption and structural performance. *Composite Structures* 200, 886–909. doi:<https://doi.org/10.1016/j.compstruct.2018.04.002>.
- [15] Sutherland, L.S., Soares, C.G., 2012. The use of quasi-static testing to obtain the low-velocity impact damage resistance of marine GRP laminates. *Composites Part B: Engineering* 43, 1459–1467. doi:[10.1016/j.compositesb.2012.01.002](https://doi.org/10.1016/j.compositesb.2012.01.002).
- [16] Tsouknidas, A., Pantazopoulos, M., Katsoulis, I., Fasnakis, D., Maropoulos, S., Michailidis, N., 2016. Impact absorption capacity of 3D-printed components fabricated by fused deposition modelling. *Materials & Design* 102, 41–44. doi:[10.1016/j.matdes.2016.03.154](https://doi.org/10.1016/j.matdes.2016.03.154).
- [17] Vangelatos, Z., Gu, G.X., Grigoropoulos, C.P., 2019. Architected metamaterials with tailored 3D buckling mechanisms at the microscale. *Extreme Mechanics Letters* 33, 100580. doi:[10.1016/j.eml.2019.100580](https://doi.org/10.1016/j.eml.2019.100580).
- [18] Wang, H., Lu, Z., Yang, Z., Li, X., 2019. A novel re-entrant auxetic honeycomb with enhanced in-plane impact resistance. *Composite Structures* 208, 758–770. doi:[10.1016/j.compstruct.2018.10.024](https://doi.org/10.1016/j.compstruct.2018.10.024).

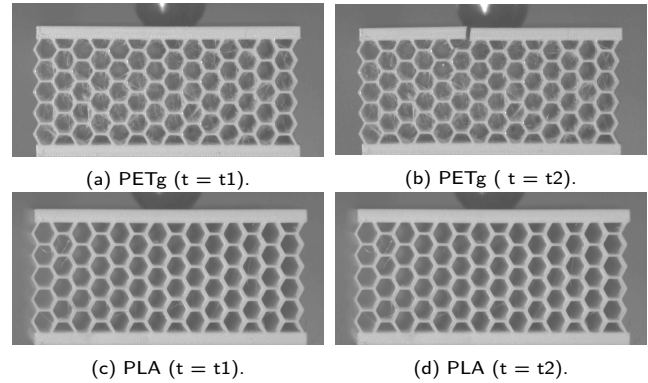


Figure 16: Low-velocity impact: 10 J (hexagonal).

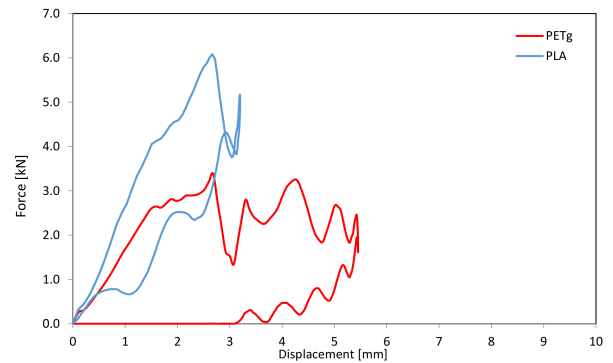


Figure 17: Force-displacement diagram: 10 J (hexagonal).

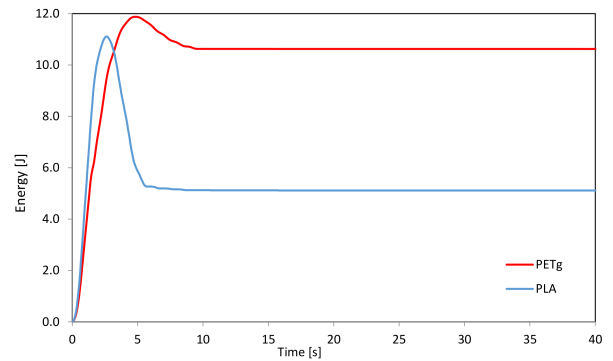


Figure 18: Energy time-history: 10 J (hexagonal).

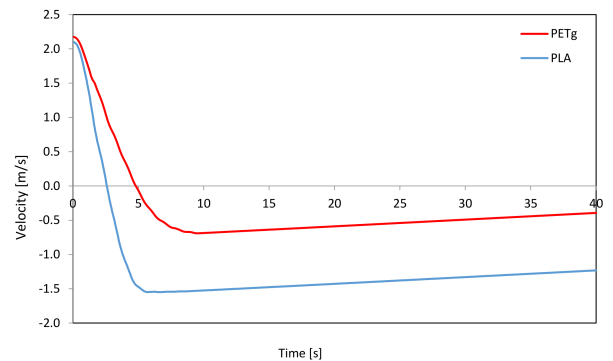


Figure 19: Velocity time-history: 10 J (hexagonal).

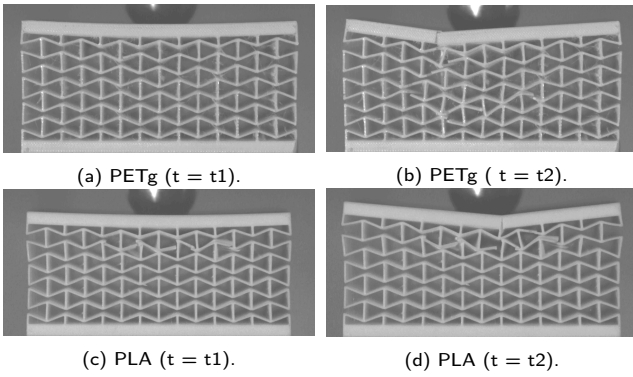


Figure 20: Low-velocity impact: 10 J (auxetic).

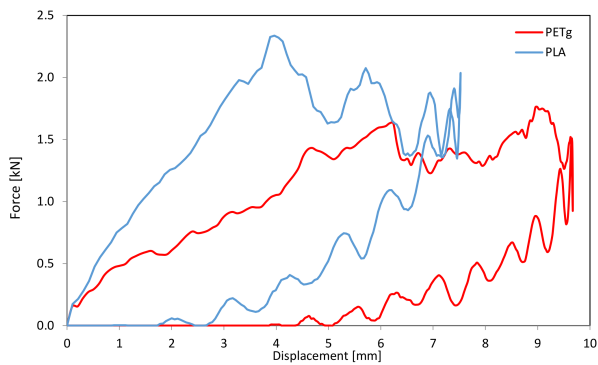


Figure 21: Force-displacement diagram: 10 J (auxetic).

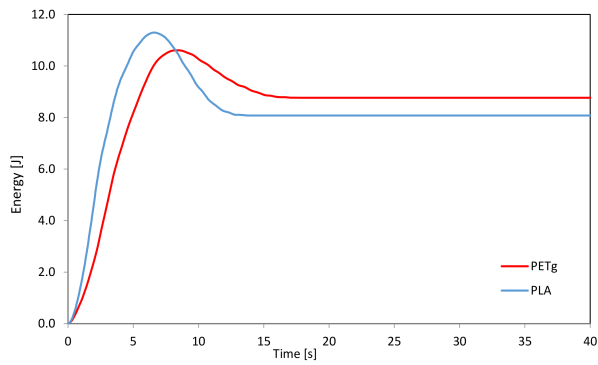


Figure 22: Energy time-history: 10 J (auxetic).

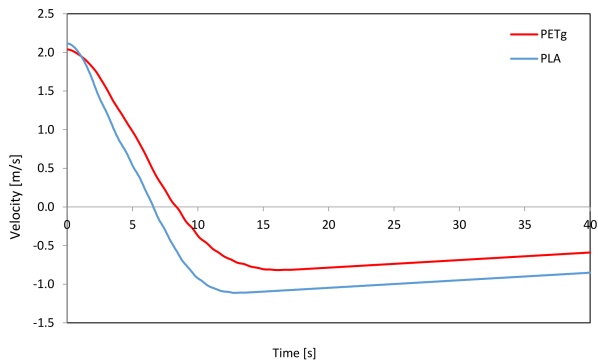


Figure 23: Velocity time-history: 10 J (auxetic).

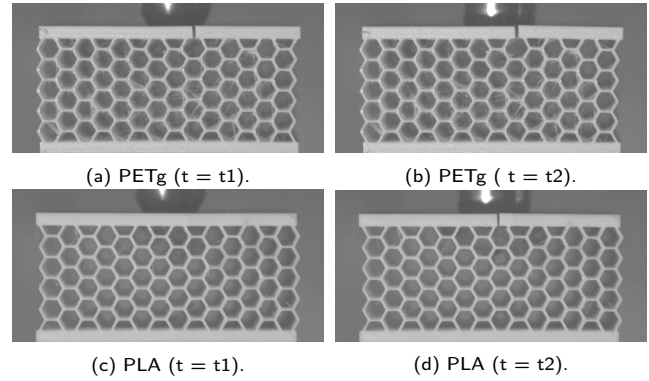


Figure 24: Low-velocity impact: 20 J (hexagonal)

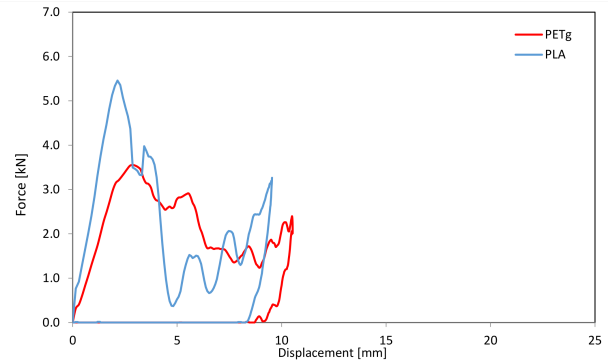


Figure 25: Force-displacement diagram: 20 J (hexagonal).

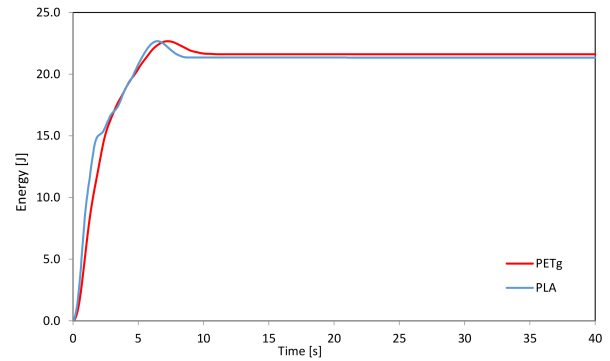


Figure 26: Energy time-history: 20 J (hexagonal).

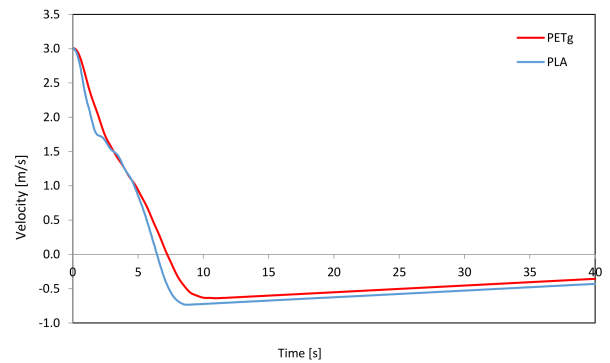


Figure 27: Velocity time-history: 20 J (hexagonal).

3D printed cellular metamaterials: PLA vs. PETg

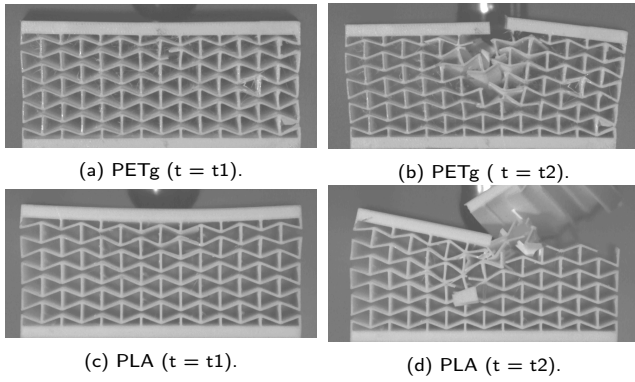


Figure 28: Low-velocity impact: 20 J (auxetic)

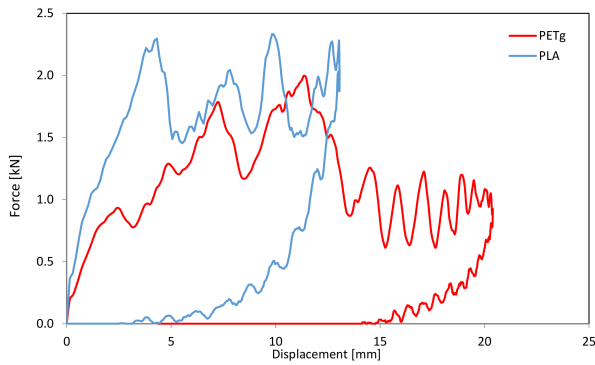


Figure 29: Force-displacement diagram: 20 J (auxetic).

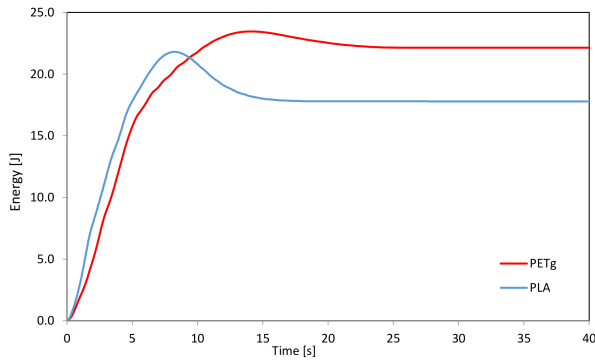


Figure 30: Energy time-history: 20 J (auxetic).

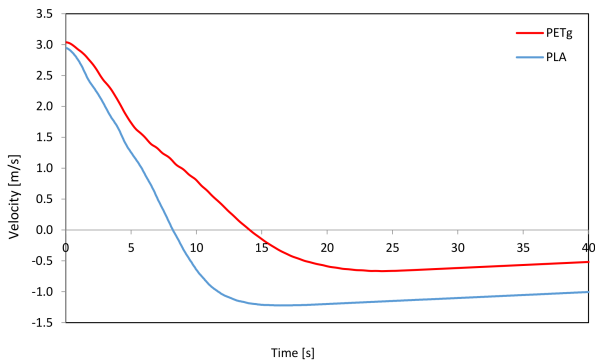


Figure 31: Velocity time-history: 20 J (auxetic).

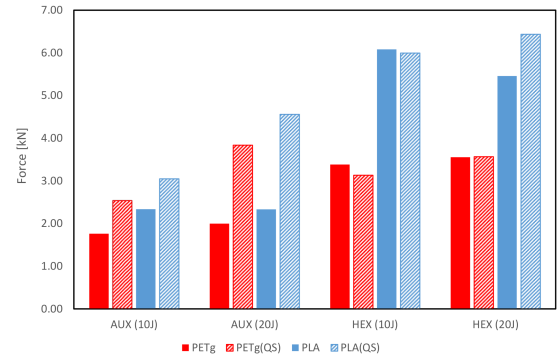


Figure 32: Maximum force.

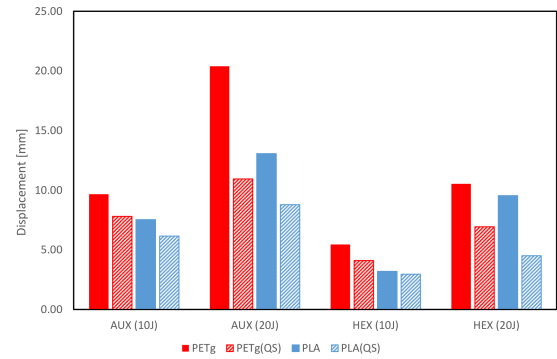


Figure 33: Maximum displacement.

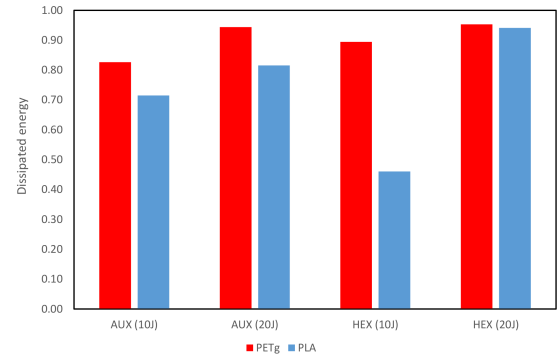


Figure 34: Ratio dissipated/absorbed energy.

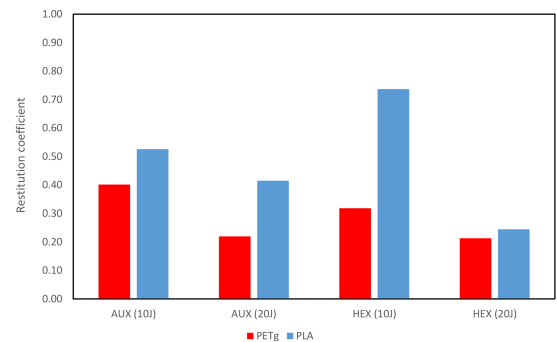


Figure 35: Restitution coefficient.